Chalcogenide perovskite $BaZrS_3$ thin-film electronic and optoelectronic devices by low temperature processing

Zhonghai Yu[a,1], Xiucheng Wei[b,1], Yixiong Zheng[c,1], Haolei Hui[b], Mengying Bian[b], Samyak Dhole[c], Jung-Hun Seo[c,*], Yi-Yang Sun[d], Quanxi Jia[c], Shengbai Zhang[e], Sen Yang[a,*], and Hao Zeng[b,*]

[a]MOE Key Laboratory for Nonequilibrium Synthesis and Modulation of Condensed Matter, Xi'an Jiaotong University, Xi'an 710049, China

[b]Department of Physics, University at Buffalo, the State University of New York, Buffalo, NY 14260, USA

[c]Department of Materials Design and Innovation, University at Buffalo, the State University of New York, Buffalo, NY 14260, USA

[d]State Key Laboratory of High Performance Ceramics and Superfine Microstructure, Shanghai Institute of Ceramics, Chinese Academy of Sciences, Shanghai 201899, China

[e]Department of Physics, Applied Physics & Astronomy, Rensselaer Polytechnic Institute, Troy, NY 12180, USA

[1] These authors contributed equally to this work.

* corresponding authors: junghuns@buffalo.edu; yangsen@mail.xjtu.edu.cn; haozeng@buffalo.edu

Abstract:

Owing to its superior visible light absorption and high chemical stability, chalcogenide perovskite barium zirconium sulfide ($BaZrS_3$) has attracted significant attention in the past few years as a potential alternative to hybrid halide perovskites for optoelectronics. However, the high processing temperatures of $BaZrS_3$ thin films at above 1000 °C severely limits their potential for device applications. Herein, we report the synthesis of $BaZrS_3$ thin films at temperatures as low as 500 °C, by changing the chemical reaction pathway. The single phase $BaZrS_3$ thin film was confirmed by X-ray diffraction and Raman spectroscopies. Atomic force microscopy and scanning electron microscopy show that crystalline size and surface roughness were consistently reduced with decreasing annealing temperature. The lower temperatures further eliminate sulfur vacancies and carbon contaminations associated with high temperature processing. The ability to synthesize chalcogenide perovskite thin films at lower temperatures removes a major hurdle for their device fabrication. The photodetectors demonstrate fast response and an on/off ratio of 80. The fabricated field effect transistors show an ambipolar behavior with electron and hole mobilities of 16.8 cm^2/Vs and 2.6 cm^2/Vs, respectively.

Keywords: chalcogenide perovskite, pulsed laser deposition, photodetector, field effect transistor

Introduction

Organic-inorganic hybrid halide perovskites have taken the center stage in photovoltaics research over the past decade [1-4], since Kojima *et al.* first introduced their application as a visible-light sensitizer in 2009 [5]. Many studies have further established their outstanding performance for optoelectronic applications, such as photodetectors [6, 7], light emitting diodes (LEDs) [8, 9], optical sensors [10, 11], and especially solar cells [12, 13]. However, the best performing halide perovskites for solar cells often contain the toxic element Pb [5, 14]. Furthermore, hybrid perovskites show inherent instability against moisture, heat, light illumination, and electric field. These disadvantages have severely impeded their commercial applications. A lot of effort has been devoted to enhancing the stability of organic perovskites, such as A-site cation engineering (*e.g.* replacing MA^+ by FA^+ and Cs^+) [15-17] and dimension reduction (*e.g.* using the two-dimensional Ruddlensden-Popper phase) [18-20].

To address the toxicity and stability limitations of hybrid perovskites, inorganic chalcogenide perovskites have been proposed as an alternative family of perovskite semiconductors for optoelectronics. In 2015, Sun *et al.* theoretically screened 18 ABX_3 chalcogenide perovskites for photovoltaics, with A as Ca/Sr/Ba, B as Ti/Zr/Hf, and X as S/Se [21]. Several ABX_3 chalcogenide perovskites were identified to have suitable band gaps and absorption properties for photovoltaics. As a prototypical chalcogenide perovskite, $BaZrS_3$ possesses a direct band gap of 1.8 eV, and strong near edge absorption [22-26]. Furthermore, $BaZrS_3$ has been shown to possess a stable perovskite structure against high pressure, moisture, and heat [23, 27]. However, little is known about its carrier transport properties as the majority of publications are on bulk powder or single crystals. We first reported the synthesis of $BaZrS_3$ thin films by high temperature (~1000 °C) sulfurization of $BaZrO_3$ films deposited via pulsed laser deposition (PLD) [28]. These films show *n*-type conductivity due to sulfur vacancies, with a carrier mobility of around 10 cm^2/Vs. Comparotto *et al.* fabricated $BaZrS_3$ thin films by co-sputtering of BaS and Zr targets, followed by a thermal treatment at temperatures varying from 650 to 1000 °C. It was reported that 900 °C was required for good crystallization. However, no transport properties were reported [29]. Gupta *et al.* synthesized $BaZrS_3$ thin films by sulfurization of $BaZrO_3$ films made by chemical solution deposition at 1050 °C [30]. Such high processing temperatures are incompatible with device fabrication, and could also lead to unintended high concentration of electron doping due to sulfur vacancy defects. Thus, lowering the processing temperature of chalcogenide perovskite thin films is a crucial step for establishing this family of materials as a viable competitor to hybrid organic perovskites for practical applications.

In this paper we report the synthesis of $BaZrS_3$ thin films at temperatures as low as 500 °C, which is comparable to the processing temperature of copper indium gallium selenide (CIGS) solar cells [31, 32]. This is achieved by changing the chemical reaction pathway from sulfurization of oxide perovskites to crystallization of pulsed laser deposited amorphous $BaZrS_x$ films. The films processed at low temperatures show stoichiometric single-phase orthorhombic perovskite structure with smooth surfaces. Elimination of excess sulfur vacancies leads to reduced carrier concentration to ~4×10^{10} cm^{-3}. As a demonstration for the potential use of the

$BaZrS_3$ thin films towards various electronic and optoelectronic applications, $BaZrS_3$ thin-film photodetectors and field effect transistors (FET) were fabricated. The photodetector measurements show photocurrent close to 2 orders of magnitude greater than dark current for the films annealed at 650 ℃. The FETs with ionic liquid (IL) gating show ambipolar behavior, with an on/off ratio of 6.5×10^3 at gate voltage of 1 V and carrier mobilities estimated to be 16.8 cm^2/Vs and 2.6 cm^2/Vs for electrons and holes, respectively. Our study paves the way for the integration of chalcogenide perovskite thin films in optoelectronic devices.

Experimental

Preparation of the $BaZrS_3$ PLD target: $BaZrS_3$ powder was synthesized from $BaZrO_3$ powder following published procedure [24]. The pre-synthesized $BaZrS_3$ powder was cold-pressed into a pellet with a 25 T hydraulic press using a circular mold of 20 mm in diameter. Before pressing, a small amount of polyvinyl alcohol (PVA) was added to enhance the adhesion and stability of the pellet. The $BaZrS_3$ pellet was sintered at 1050 ℃ in Ar atmosphere for 2 hours, and used as target for PLD.

Synthesis of $BaZrS_3$ thin films: A 1 cm×1 cm (0001) sapphire wafer was loaded into the ultrahigh vacuum (UHV) deposition chamber of the PLD system equipped with a KrF pulsed excimer laser (λ=248 nm), at a base pressure of 1×10^{-8} torr. The substrate holder was kept at temperatures of 500-700 ℃ during the deposition, with a laser repetition rate of 5 Hz and laser fluence of 5 J/cm^2. During the deposition, the substrate and target were both rotated at 30 rpm to ensure homogeneity of the films. The as-grown amorphous $BaZrS_x$ thin films were cooled down to room temperature in the UHV chamber and then transferred to an MTI two-zone tube furnace in a 2-inch diameter quartz tube for annealing under CS_2 carried by Ar gas flow at 12 standard cubic centimeters. The heating profile and a sketch of the setup are shown in the supporting information (SI) Fig S1. The as-deposited thin films were placed at the center of zone 2 downstream, with temperatures ranging from 500 to 900 ℃ and corresponding total annealing time ranging from 2 to 8 hours. The temperature of zone 1 was kept at 900 ℃ for complete decomposition of CS_2, as the decomposition rate of CS_2 is highly temperature dependent [33].

Thin film characterizations: The X-ray Diffraction (XRD) θ-2θ scans were performed using an X'pert Pro X-ray diffractometer operating at 1.6 kW (Cu Kα radiation). Raman spectra were obtained from a HORIBA Raman spectrometer working under 532 nm laser excitation. The scanning electron microscopy (SEM) images and energy dispersive X-ray spectroscopy (EDX) analysis were acquired from a Focused Ion Beam-Scanning Electron Microscope (FIB-SEM) – Carl Zeiss AURIGA CrossBeam with an Oxford EDS system. The Bruker AXS-Innova atomic force microscope (AFM) was used to obtain the surface roughness and thickness profiles. The absorption spectra were collected from a Cary series UV-Vis-NIR spectrophotometer measured from 400 nm to 800 nm.

Device fabrication and Characterization: The photodetector devices were fabricated by depositing the source and drain electrodes by electron beam evaporation of a 30 nm thick Au film through a shadow mask, with a deposition rate of 0.4 Å/s, using an AJA Dual ATC-Orion

UHV system with a base pressure of 1×10^{-8} torr. The photodetector has a channel width of 1000 μm and a gap of 50 μm. The I-V curves were measured by a Keithley 4200-SCS Semiconductor Parameter Analyzer, in the dark and under illumination with an excitation wavelength of 532 nm and light intensity of 0.14 W/cm^2. The FET devices were fabricated by the same technique through a T-shaped mask. The FET has a channel length of 50 μm and a width of 1000 μm. The side gate is separated from the source and drain electrodes by a 150 μm gap. A drop of the IL Diethylmethyl(2-methoxyethyl)ammoniumbis(trifluoromethylsulfonyl)imide (DEME-TFSI), about 20 μL, was dispensed to cover the active area of the $BaZrS_3$ FET. The device was baked at 120 ℃ for 12 hours in a N_2 glove box to remove any moisture in the IL. The drain-source current I_{DS} as a function of drain-source voltage V_{DS} under different gate voltages V_G and drain-gate capacitance C_{DG} vs drain-gate voltage V_G were measured by a Keithley 4200-SCS Semiconductor Parameter Analyzer.

Results and discussions

Conventional semiconductors and oxide/halide perovskites represent two ends of the spectrum in terms of the covalency-iconicity duality. Chalcogenide perovskites clearly belong to the ionic side of the spectrum, in stark contrast to conventional four-fold coordinated semiconductors. As a crude quantification of the effective ionicity/covalency, one may calculate the Pauling electronegativity (χ) difference per anion [34]. For $BaZrS_3$, $\Delta\chi = \frac{[3\chi(S)-\chi(\mathrm{Ba})-\chi(\mathrm{Zr})]}{3} = 1.84$ eV. Using the same methodology, $\Delta\chi$ is found to be 1.43 eV for AlN and 0.37 eV for GaAs. To put it into perspective, $BaZrS_3$ has a moderate band gap of 1.8 eV, close to that of GaAs; but its effective ionicity is even higher than that of wide gap AlN with a band gap of 6 eV. Possessing a moderate band gap with an exceptionally large ionicity puts $BaZrS_3$ and other chalcogenide perovskites in a unique category of defect tolerant semiconductors that may offer new opportunities for electronic and optoelectronic applications.

The high processing temperature of $BaZrS_3$ thin films in earlier studies was mainly attributed to the chemical reaction pathways with high activation barriers. As both group IIA and group IVB elements in perovskites have low electronegativity, their oxides are very stable and difficult to be converted into chalcogenides. In the approach of co-sputtering of BaS/Zr [29], the high processing temperature above 900 °C may also be related to the difficulty of the chemical reaction between BaS and Zr, as Zr is a refractory metal with a high melting point of 1855 °C. The residual oxides during the handling may further exacerbate the formation of $BaZrS_3$ using sulfur. Therefore, to reduce the processing temperature, a change of the reaction pathway is necessary. PLD has been used to deposit a wide range of compounds including oxides, nitrides and carbides [35-37]. PLD is also known to be able to keep the stoichiometry of the target material under optimal conditions [38]. Postulating that by PLD deposition of a stoichiometric $BaZrS_3$ compound target under optimal conditions, $BaZrS_3$ perovskite thin films can be obtained under milder conditions.

We found that the stoichiometry of the Ba:Zr cations of the as-deposited films is dependent on laser fluence of the PLD system. This effect can be understood as primarily due to the large difference in the cohesive energy of Ba vs. Zr (1.9 eV/atom vs. 6.25 eV/atom). Therefore, low laser fluence is expected to result in Ba-rich films, while very high laser fluence may result in Ba deficiency due to reverse sputtering. Under a narrow window of fluence of close to 5 J/cm^2, a 1:1 ratio of Ba:Zr was obtained, as shown in Fig S2(a), However, it was found that the as-deposited films were amorphous, even with an in-situ substrate temperature as high as 700 °C (Fig S3). It was further determined that these films are highly sulfur deficient, with a composition of $BaZrS_{2.4}$, as shown by the EDX spectroscopy results (Fig S2(b)), which perhaps contributes to their poor crystallinity.

To obtain stoichiometric, single phase $BaZrS_3$ in the orthorhombic perovskite structure, thermal annealing of the as-deposited amorphous $BaZrS_{2.4}$ films in CS_2 at various temperatures ranging from 500 ℃ to 900 ℃ were performed in a two-zone tube furnace. All of the $BaZrS_3$ films after annealing appeared dark red in color (see optical images in Fig 1(b)), except the one annealed at 500 °C, indicating strong visible light absorption. The 500 °C sample does show lighter color,

suggesting incomplete crystallization. The sulfur concentration as measured by EDX is annealing temperature dependent, as seen in Fig S4. While as-deposited $BaZrS_{2.4}$ films are sulfur deficient, the composition of the films progressively approaches perfect stoichiometry of Ba:Zr:S=1:1:3 with decreasing annealing temperature. To investigate the annealing temperature dependent structural evolution of the $BaZrS_3$ films, XRD θ-2θ scans were performed for films annealed at 900 ℃, 850 ℃, 650 ℃, 550 ℃, and 500 ℃, respectively, as shown in Fig 1(a). The peaks labeled with Miller indices indicate standard peak positions of $BaZrS_3$ with a Pnma structure, retrieved from the PDF card JCPDS 00-015-0327. It is found that all discernible peaks for the samples annealed from 500 to 900 °C match well with the reference. No additional peaks were observed, suggesting that the obtained films were of a single phase. Some diffraction peaks with low intensities were not clearly observed from films annealed at 550 ℃ and 500 ℃, as a result of low crystallinity and small grain sizes at such low temperatures. As can be seen from Fig 1(b), the full width at half maximum (FWHM) of the (121) diffraction peak decreases from 0.62° to 0.45° with increasing annealing temperatures from 550 ℃ to 900 ℃. The crystallite sizes as calculated from Scherrer's formula using the FWHM of the (121) diffraction peak decreases monotonically with decreasing annealing temperature. The lateral grain sizes, as imaged by AFM and SEM (shown in Fig 2(a)-(h) and Fig S5) also decreases monotonically from ~110 nm at 900 ℃ to 35 nm at 550 ℃. It is interesting to note that the lateral grain sizes are several times larger than the vertical grain sizes. Understanding the detailed crystallization mechanisms in the future will help to obtain films with enhanced grain size and crystallinity.

The surface roughness of a semiconductor thin films plays an important role in determining the interface quality, carrier transport in junctions, and thus device performance [39, 40]. It is expected that a lower annealing temperature with smaller crystallite size should also possess lower surface roughness. The AFM top-view images in Fig 2(a)-2(d) and 3D topography images displayed in Fig 2(e) -2(h) show clearly that the crystallite size and surface roughness of the $BaZrS_3$ thin films decreases consistently with decreasing annealing temperature from 900 ℃ to 550 ℃, respectively. The height profile measured along a scan length of 5 μm for different annealing temperatures is shown in Fig 2(i). The root mean square (RMS) of the surface roughness R_q decreases by 20 folds from 10.5 nm at annealing temperature of 900 ℃ to 0.59 nm at annealing temperature of 650 ℃, as seen in Fig 2(j). This trend can be explained by the consequence of a decrease in grain size with decreasing annealing temperature.

The room temperature Raman spectra of $BaZrS_3$ films annealed at 900 ℃, 850 ℃, 650 ℃, and 550 ℃ are shown in Fig 3(a). Several peaks can be identified in the range of 50 cm^{-1} to 500 cm^{-1} and six of them are assigned to be B_{1g}^1, A_g^4, B_{2g}^6, B_{1g}^4, B_{1g}^5 and B_{3g}^5 vibrational modes calculated theoretically for $BaZrS_3$ with the Pnma structure [27]. The Raman spectra measured at low temperature (100K) are provided in Supporting Information Fig. S6. In addition, we measured the Raman spectra at higher wavenumbers between 1000 cm^{-1} and 2000 cm^{-1} for all the films to investigate the possibility of carbon contamination resulting from CS_2 decomposition. As can be seen from Fig. 3(b), for the film annealed at 900 °C, two peaks at 1330 and 1620 cm^{-1} were observed, which can be attributed to the D and G bands of carbon materials such as graphite and nano-diamonds. While these modes are barely observable for the sample annealed at 850 °C, they are absent in the films annealed at and below 650 °C. This

suggests that carbon contamination has been eliminated by low temperature processing. The presence of carbon also explains the color difference of $BaZrS_3$ processed at different temperatures: while the films processed at 1050 °C show black color (not shown), the films processed at 900 °C and below are dark red.

$BaZrS_3$ thin films annealed at 650 °C and 900 °C were selected for UV-vis absorption measurements to examine their optical properties. The thicknesses of these films are about 280 nm, as measured by AFM (Fig 4(a)). The absorption spectra are shown in Fig 4 (b). It can be seen that their absorption coefficient α above the band gap are ~ 5×10^4 and ~ 6×10^4 cm^{-1}, respectively. These values are somewhat smaller than that of $BaZrS_3$ films processed at higher temperatures [28]. A linear fitting near the band edge of the Tauc plot results in a band gap value of 1.98 and 1.86 eV, respectively, for the films annealed at 650 °C and 900 °C, respectively, as shown in Fig 4(c). These values are slightly higher than the band gap in the films processed at 1050 °C. Several factors could contribute to these differences: 1. The presence of a minute amount of amorphous oxides/oxysulfides, possibly introduced in the target processing, could not be completely eliminated in low temperature processing. The wide gap oxides/oxysulfides may lead to an overestimate of the band gap, as well as lower the absorption coefficient. Careful examination of XRD patterns of samples processed at different temperatures (Fig. 1(a)) reveals no oxide peaks or shift of the peaks compared to the $BaZrS_3$ standard, within the instrument limit. This rules out the presence of measurable amount of crystalline oxides or oxysulfides; 2. The presence of carbon contamination in previous high temperature processed samples may lead to overestimate of the absorption coefficient and underestimate of band gap, as carbon absorbs in a broad range of wavelengths; 3. We observed a small but noticeable shift of the Raman peaks to higher wavenumbers at higher processing temperatures (Fig. S6). While presence of oxysulfides could lead to shift of Raman modes to higher frequencies, this is inconsistent with the fact that this shift is for samples processed at higher temperatures and therefore conversion to the $BaZrS_3$ phase is more complete. We suggest that a slight difference in structural distortion (octahedron rotation) at different processing temperatures is responsible for the observed Raman shift, which could contribute to subtle differences in electronic structures and band gaps [41].

In summary, lower temperature growth of $BaZrS_3$ results in stoichiometric films with minimized concentration of sulfur vacancies, eliminated carbon contamination, smaller crystallite sizes and lower surface roughness. These are expected to strongly affect the carrier transport characteristics and device performance. To investigate the influence of film microstructure on carrier transport, we fabricated and measured photodetector and FET devices using the $BaZrS_3$ films annealed at different temperatures as active semiconductors.

The I-V curves of the photodetector devices were measured in the dark and under illumination, for films annealed at temperatures of 850 °C, 650 °C, and 550 °C, respectively, as shown in Fig 5(a) to 5(c). An optical image of the device is shown in the inset of Fig 5(a). At 850 °C, the I-V curves show little difference under dark and illumination. This suggests that carriers available for the transport are essentially intrinsic to the material, and the contribution from the photo-generated carriers to the transport is negligible. The high dark current can be attributed to the

high concentration of sulfur vacancies, as each sulfur vacancy can donate two electrons. Using the sulfur vacancy concentration measured by EDX (Fig S4), we estimate the carrier density to be 1.7×10^{21} cm^{-3}. For the film annealed at 650 ℃, the measured photocurrent is 80 times greater than the dark current, as can be seen in Fig 5(b). The film annealed at 550 ℃ shows the highest photocurrent of 17 nA at 10 V. However, the on/off ratio is only 20 times due to the relatively higher dark current. The relatively higher dark current could be caused by the lower crystallinity, where a number of defects may be present and contribute to excess carriers, as shown by our unpublished theoretical study [42]. The photo responsivity is calculated to be 0.08 mA/W at a bias voltage of 5V for the films annealed at 550 ℃. The moderate photo response is primarily due to the relatively small grain sizes, which leads to significant carrier scattering and limits the carrier mobility. In Fig 5(d), we plot the photocurrent as a function of time for the films annealed at 650 ℃ under periodically switched light source at a fixed bias voltage of 8 V. The device shows fast response and low rise/fall time. Due to instrument limit, we estimate the upper limit of the response time to be 0.3 ms. However, the actual response time could be much smaller. The I-V curves measured at different excitation wavelengths for films annealed at 650 ℃ are plotted in Fig 5(e), and the wavelength dependent photocurrent at bias voltages of 3, 5 and 8 V are shown in Fig 5(f). The device shows the highest photo response at the excitation wavelength around 500 nm. The cutoff wavelength is found to be about 670 nm. This confirms the band gap of the $BaZrS_3$ film annealed at 650 ℃ to be about 1.85 eV. This suggests that the UV-vis absorption measurements slightly overestimate the band gap, perhaps due to the small amount of oxides.

FET devices were fabricated using the film annealed at 650 ℃ to further study the carrier transport, using an IL side gate, as shown by the optical image in the inset of Fig 6(a). The drain-source current I_{DS} as a function of bias voltage V_{DS}, measured at positive and negative gate voltages V_G are shown in Fig 6(a) and (b), respectively. The total specific capacitance of the IL is determined by the capacitance of the electrical double layer (EDL), and can reach as high as ~20 $\mu F/cm^2$ [43], which makes it possible to generate high electric field of ~ 10 MV/cm at low gate voltages [44], comparing to commonly used metal oxide dielectric such as SiO_2, Al_2O_3 or HfO_2. At a V_{DS} of 1 V, I_{DS} is measured to be 3×10^{-11} A without gating, which suggests very small intrinsic carrier density. The intrinsic carrier type is found to be n-type, which is consistent with our previous work [28]. The intrinsic carrier concentration is found to be 4.4×10^{10} cm^{-3}. These results further confirm that carrier concentration is suppressed by reducing the density of sulfur vacancies in $BaZrS_3$ films processed at low temperatures. With increasing V_G to 1V, I_{DS} reaches to 2×10^{-7} A, resulting in an ON/OFF ratio of 6.5×10^3. Similar but smaller I_{DS} can be observed for negative V_G, as shown in Fig 6(b), suggesting ambipolar behavior in our FETs. We further estimate the electron and hole mobilities to be 16.8 cm^2/Vs and 2.6 cm^2/Vs, respectively, from the saturated I_{DS} vs. V_G data. The capacitance of the IL layer used in the calculation was obtained from the C-V measurements. The carrier mobility is primarily limited by the small grain sizes which contribute to substantial carrier scattering. Future work should focus on improving the grain size of $BaZrS_3$ films processed at low temperatures to improve the performance of electronic and optoelectronic devices.

Conclusion

In conclusion, we have obtained polycrystalline perovskite $BaZrS_3$ thin films, by low temperature crystallization of PLD deposited amorphous $BaZrS_x$ films in CS_2. The films with good crystallinity and a surface roughness smaller than 0.6 nm can be obtained at processing temperatures as low as 550 ℃. The low processing temperatures result in the elimination of both excessive carriers due to vacancy formation and carbon contamination. Prototype photodetector devices fabricated with such films show good visible light sensitivity, and their wavelength dependent photo response confirms a band gap of ~ 1.85 eV. The FET indicates ambipolarity of the charge carriers, with electron and hole mobilities of 16.8 cm^2/Vs and 2.6 cm^2/Vs, respectively. Our findings will expedite the progress towards applications of $BaZrS_3$ and other chalcogenide perovskites for electronics and optoelectronics.

Author contributions

Z.Y. synthesized the PLD target and thin films, and performed structural and optical characterizations. X.W. fabricated the photodetector and FET devices. X.W. and Y.Z. performed device characterizations and data analysis. H. Z. conceived the idea. S.Y., J.S. and H.Z. supervised the project. X.W., Z.Y. and H.Z. wrote the manuscript. All authors discussed the results and contributed to the final manuscript.

Acknowledgements

Work supported by US NSF CBET-1510121, CBET-1510948, MRI- 1229208, and DOE DE-EE0007364. Z. Yu and S. Yang acknowledge NSFC (Grant No. 91963111) and Key Scientific and Technological Innovation Team of Shaanxi Province (2020TD-001). Y. -Y.S. acknowledges support by NSFC under Grant 11774365.

Conflict of Interest

The authors declare no conflict of interest.

References

[1] N. J. Jeon, J. H. Noh, W. S. Yang, Y. C. Kim, S. Ryu, J. Seo, S. I. Seok, Compositional engineering of perovskite materials for high-performance solar cells, *Nature* **517** (2015) 476-480.

[2] M. Liu, M. B. Johnston, H. J. Snaith, Efficient planar heterojunction perovskite solar cells by vapour deposition, *Nature* **501** (2013) 395.

[3] M. M. Lee, J. Teuscher, T. Miyasaka, T. N. Murakami, H. J. Snaith, Efficient hybrid solar cells based on meso-superstructured organometal halide perovskites, *Science* **338** (2012) 643-647.

[4] G. Xing, N. Mathews, S. Sun, S. S. Lim, Y. M. Lam, M. Grtzel, S. Mhaisalkar, T. C. Sum, Long-Range Balanced Electronand Hole-Transport Lengths in Organic-Inorganic CH3NH3PbI3, *Science* **342** (2013) 344.

[5] A. Kojima, K. Teshima, Y. Shirai, T. Miyasaka, Organometal Halide Perovskites as Visible-Light Sensitizers for Photovoltaic Cells, *J. Am. Chem. Soc.* **131** (2009) 6050-6051.

[6] Y. H. Lee, I. Song, S. H. Kim, J. H. Park, S. O. Park, J. H. Lee, Y. Won, K. Cho, S. K. Kwak, J. H. Oh, Perovskite Photodetectors: Perovskite Granular Wire Photodetectors with Ultrahigh Photodetectivity (Adv. Mater. 32/2020), *Advanced Materials* **32** (2020) 2070238.

[7] W. Tian, H. Zhou, L. Li, Hybrid organic–inorganic perovskite photodetectors, *Small* **13** (2017) 1702107.

[8] Q. Shan, J. Song, Y. Zou, J. Li, L. Xu, J. Xue, Y. Dong, B. Han, J. Chen, H. Zeng, High performance metal halide perovskite light-emitting diode: from material design to device optimization, *Small* **13** (2017) 1701770.

[9] Y. H. Kim, S. Kim, S. H. Jo, T. W. Lee, Metal Halide Perovskites: From Crystal Formations to Light-Emitting-Diode Applications, *Small Methods* **2** (2018) 1800093.

[10] C. N. Rao, P. Dua, P. Kuchhal, Y. Lu, S. Kale, P. Cao, Enhanced sensitivity of magneto-optical sensor using defect induced perovskite metal oxide nanomaterial, *Journal of Alloys and Compounds* **797** (2019) 896-901.

[11] C. Y. Wu, Z. Wang, L. Liang, T. Gui, W. Zhong, R. C. Du, C. Xie, L. Wang, L. B. Luo, Graphene-Assisted Growth of Patterned Perovskite Films for Sensitive Light Detector and Optical Image Sensor Application, *Small* **15** (2019) 1900730.

[12] S. Yang, S. Chen, E. Mosconi, Y. Fang, X. Xiao, C. Wang, Y. Zhou, Z. Yu, J. Zhao, Y. Gao, Stabilizing halide perovskite surfaces for solar cell operation with wide-bandgap lead oxysalts, *Science* **365** (2019) 473-478.

[13] N. Ito, M. A. Kamarudin, D. Hirotani, Y. Zhang, Q. Shen, Y. Ogomi, S. Iikubo, T. Minemoto, K. Yoshino, S. Hayase, Mixed Sn–Ge perovskite for enhanced perovskite solar cell performance in air, *The journal of physical chemistry letters* **9** (2018) 1682-1688.

[14] M. L. Agiorgousis, Y.-Y. Sun, H. Zeng, S. Zhang, Strong Covalency-Induced Recombination Centers in Perovskite Solar Cell Material CH3NH3PbI3, *J. Am. Chem. Soc.* **136** (2014) 14570-14575.

[15] M. Kulbak, S. Gupta, N. Kedem, I. Levine, T. Bendikov, G. Hodes, D. Cahen, Cesium enhances long-term stability of lead bromide perovskite-based solar cells, *The journal of physical chemistry letters* **7** (2016) 167-172.
[16] F. C. Hanusch, E. Wiesenmayer, E. Mankel, A. Binek, P. Angloher, C. Fraunhofer, N. Giesbrecht, J. M. Feckl, W. Jaegermann, D. Johrendt, Efficient planar heterojunction perovskite solar cells based on formamidinium lead bromide, *The journal of physical chemistry letters* **5** (2014) 2791-2795.
[17] C. C. Boyd, R. Cheacharoen, T. Leijtens, M. D. McGehee, Understanding degradation mechanisms and improving stability of perovskite photovoltaics, *Chemical reviews* **119** (2018) 3418-3451.
[18] L. N. Quan, M. Yuan, R. Comin, O. Voznyy, E. M. Beauregard, S. Hoogland, A. Buin, A. R. Kirmani, K. Zhao, A. Amassian, Ligand-stabilized reduced-dimensionality perovskites, *Journal of the American Chemical Society* **138** (2016) 2649-2655.
[19] F. A. Roghabadi, M. Alidaei, S. M. Mousavi, T. Ashjari, A. S. Tehrani, V. Ahmadi, S. M. Sadrameli, Stability progress of perovskite solar cells dependent on the crystalline structure: From 3D ABX 3 to 2D Ruddlesden–Popper perovskite absorbers, *Journal of Materials Chemistry A* **7** (2019) 5898-5933.
[20] Y.-W. Jang, S. Lee, K. M. Yeom, K. Jeong, K. Choi, M. Choi, J. H. Noh, Intact 2D/3D halide junction perovskite solar cells via solid-phase in-plane growth, *Nature Energy* 1-9.
[21] Y.-Y. Sun, M. L. Agiorgousis, P. Zhang, S. Zhang, Chalcogenide perovskites for photovoltaics, *Nano letters* **15** (2015) 581-585.
[22] W. Meng, B. Saparov, F. Hong, J. Wang, D. B. Mitzi, Y. Yan, Alloying and defect control within chalcogenide perovskites for optimized photovoltaic application, *Chemistry of Materials* **28** (2016) 821-829.
[23] X. Wei, H. Hui, S. Perera, A. Sheng, D. F. Watson, Y.-Y. Sun, Q. Jia, S. Zhang, H. Zeng, Ti-alloying of BaZrS3 chalcogenide perovskite for photovoltaics, *ACS Omega* (2020).
[24] S. Perera, H. Hui, C. Zhao, H. Xue, F. Sun, C. Deng, N. Gross, C. Milleville, X. Xu, D. F. Watson, B. Weinstein, Y.-Y. Sun, S. Zhang, H. Zeng, Chalcogenide perovskites – an emerging class of ionic semiconductors, *Nano Energy* **22** (2016) 129-135.
[25] S. Niu, H. Huyan, Y. Liu, M. Yeung, K. Ye, L. Blankemeier, T. Orvis, D. Sarkar, D. J. Singh, R. Kapadia, J. Ravichandran, Bandgap Control via Structural and Chemical Tuning of Transition Metal Perovskite Chalcogenides, *Advanced Materials* **29** (2017) 1604733.
[26] Y. Nishigaki, T. Nagai, M. Nishiwaki, T. Aizawa, M. Kozawa, K. Hanzawa, Y. Kato, H. Sai, H. Hiramatsu, H. Hosono, Extraordinary Strong Band-Edge Absorption in Distorted Chalcogenide Perovskites, *Solar RRL* (2020) 1900555.
[27] N. Gross, Y.-Y. Sun, S. Perera, H. Hui, X. Wei, S. Zhang, H. Zeng, B. Weinstein, Stability and Band-Gap Tuning of the Chalcogenide Perovskite BaZrS 3 in Raman and Optical Investigations at High Pressures, *Physical Review Applied* **8** (2017) 044014.
[28] X. Wei, H. Hui, C. Zhao, C. Deng, M. Han, Z. Yu, A. Sheng, P. Roy, A. Chen, J. Lin, D. F. Watson, Y.-Y. Sun, T. Thomay, S. Yang, Q. Jia, S. Zhang, H. Zeng, Realization of BaZrS3 chalcogenide perovskite thin films for optoelectronics, *Nano Energy* **68** (2020) 104317.

[29] C. Comparotto, A. Davydova, T. Ericson, L. Riekehr, M. V. Moro, T. Kubart, J. Scragg, Chalcogenide Perovskite BaZrS3: Thin Film Growth by Sputtering and Rapid Thermal Processing, *ACS Applied Energy Materials* **3** (2020) 2762-2770.
[30] T. Gupta, D. Ghoshal, A. Yoshimura, S. Basu, P. K. Chow, A. S. Lakhnot, J. Pandey, J. M. Warrender, H. Efstathiadis, A. Soni, An Environmentally Stable and Lead-Free Chalcogenide Perovskite, *Advanced Functional Materials* **30** (2020) 2001387.
[31] H. Liang, U. Avachat, W. Liu, J. van Duren, M. Le, CIGS formation by high temperature selenization of metal precursors in H2Se atmosphere, *Solid-state electronics* **76** (2012) 95-100.
[32] L. Lin, N. M. Ravindra, CIGS and perovskite solar cells–an overview, *Emerging Materials Research* **9** (2020) 812-824.
[33] T. C. Peng, Carbon disulfide dissociation in a thermal cell, *The Journal of Physical Chemistry* **78** (1974) 634-638.
[34] L. Pauling, The nature of the chemical bond. IV. The energy of single bonds and the relative electronegativity of atoms, *Journal of the American Chemical Society* **54** (1932) 3570-3582.
[35] D. Benetti, R. Nouar, R. Nechache, H. Pepin, A. Sarkissian, F. Rosei, J. MacLeod, Combined magnetron sputtering and pulsed laser deposition of TiO2 and BFCO thin films, *Scientific reports* **7** (2017) 1-9.
[36] E. Paneerselvam, V. K. L. Narayanan, N. J. Vasa, M. Higashihata, D. Nakamura, H. Ikenoue, M. R. Rao, Laser Assisted Doping of Silicon Carbide Thin Films Grown by Pulsed Laser Deposition, *Journal of Electronic Materials* **48** (2019) 3468-3478.
[37] G. Wisz, I. Virt, P. Sagan, P. Potera, R. Yavorskyi, Structural, optical and electrical properties of Zinc Oxide layers produced by pulsed laser deposition method, *Nanoscale Research Letters* **12** (2017) 253.
[38] C. Yu, A. S. Sokolov, P. Kulik, V. G. Harris, Stoichiometry, phase, and texture evolution in PLD-Grown hexagonal barium ferrite films as a function of laser process parameters, *Journal of Alloys and Compounds* **814** (2020) 152301.
[39] A. Pirovano, A. L. Lacaita, G. Ghidini, G. Tallarida, On the correlation between surface roughness and inversion layer mobility in Si-MOSFETs, *IEEE Electron Device Letters* **21** (2000) 34-36.
[40] Z. Liang, K. Sasikumar, P. Keblinski, Thermal transport across a substrate–thin-film interface: effects of film thickness and surface roughness, *Physical review letters* **113** (2014) 065901.
[41] C. Ming, K. Yang, H. Zeng, S. Zhang, Y.-Y. Sun, Octahedron rotation evolution in 2D perovskites and its impact on optoelectronic properties: the case of Ba–Zr–S chalcogenides, *Materials Horizons* **7** (2020) 2985-2993.
[42] X. Wu, W. Gao, J. Chai, C. Ming, M. Chen, H. Zeng, P. Zhang, S. Zhang, Y.-Y. Sun, Defect tolerance in chalcogenide perovskite BaZrS3: Effect of Hubbard U and Hartree-Fock exchange, *to be published* (2021).
[43] E. Said, X. Crispin, L. Herlogsson, S. Elhag, N. D. Robinson, M. Berggren, Polymer field-effect transistor gated via a poly (styrenesulfonic acid) thin film, *Applied Physics Letters* **89** (2006) 143507.
[44] K. Prassides, Superconductivity at the double, *Nature nanotechnology* **6** (2011) 400-401.

Figures captions

Figure 1. (a) XRD patterns of $BaZrS_3$ films annealed at different temperatures. (b) The FWHMs of the (121) peak as a function of annealing temperature. The inset shows the optical images of the $BaZrS_3$ films annealed at the respective temperatures.

Figure 2. AFM top-view and 3D topographic images of $BaZrS_3$ thin films annealed at (a) and (e) 900 ℃, (b) and (f) 850 ℃, (c) and (g) 650 ℃, and (d) and (h) 550 ℃. (i) The height profile measured along a scan length of 5 μm. (j) The root mean square (RMS) surface roughness R_q as a function of annealing temperature.

Figure 3. (a) The room temperature Raman spectra of $BaZrS_3$ films annealed at different temperatures. (b) Raman spectra at higher wavenumbers showing presence/absence of carbon contamination.

Figure 4. (a) The AFM height profiles, (b) The absorption coefficient, and (c) The Tauc plot of the films annealed at 650 ℃ and 900 ℃, respectively.

Figure 5. The I-V curves in dark and under illumination of the photodetectors fabricated from the films annealed at (a) 850 ℃, (b) 650 ℃, and (c) 550 ℃. The inset in (a) is an optical image of the device. (d) Current vs time for the device using the film annealed at 650 ℃, with a periodically switched light source (532 nm) at the fixed bias of 8 V. (e) The I-V curves measured at different excitation wavelengths for the device in (d). (f) The wavelength dependent photocurrent at bias voltages of 3, 5 and 8 V extracted from (e).

Figure 6. The I_{DS} vs V_{DS} of the FET fabricated using the film annealed at 650 ℃ under (a) positive and (b) negative gate voltages V_G. The inset in (a) is an optical image of the FET with IL side-gate.

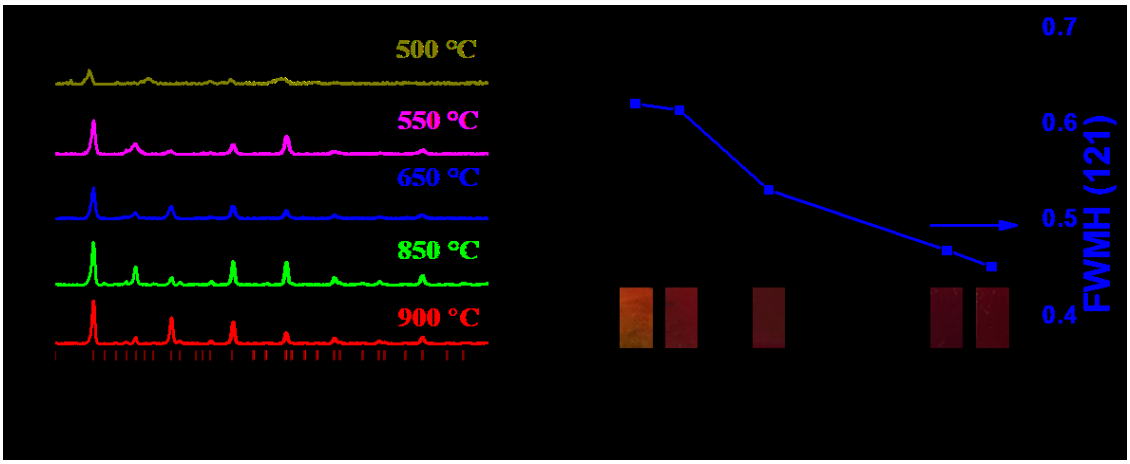

Figure. 1

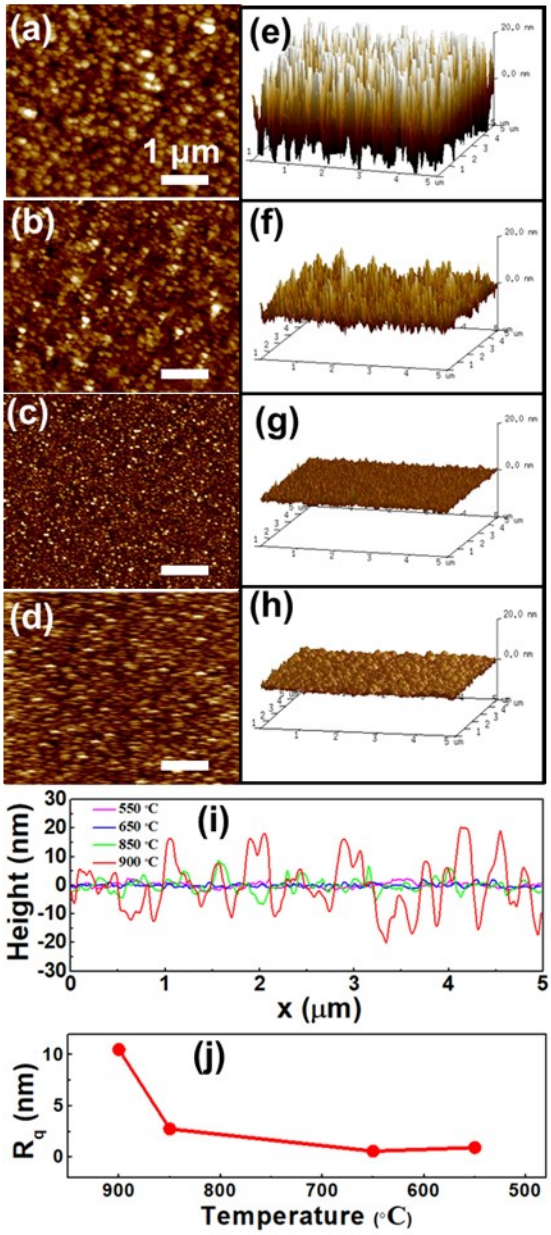
(a)
1 μm
(b)
(c)
(d)
(e)
(f)
(g)
(h)
(i)
550 °C
650 °C
850 °C
900 °C
Height (nm)
x (μm)
(j)
R_q (nm)
Temperature (°C)

Figure 2

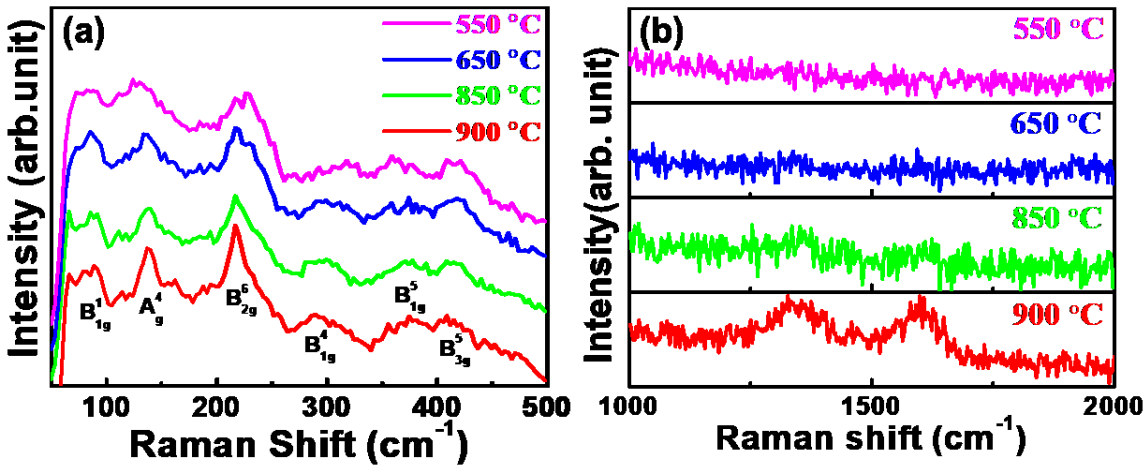
(a)
550 °C
650 °C
850 °C
900 °C
Intensity (arb.unit)
B^1_{1g}
A^4_g
B^6_{2g}
B^4_{1g}
B^5_{1g}
B^5_{3g}
100
200
300
400
500
Raman Shift (cm^{-1})
(b)
550 °C
650 °C
850 °C
900 °C
Intensity(arb. unit)
1000
1500
2000
Raman shift (cm^{-1})

Figure 3

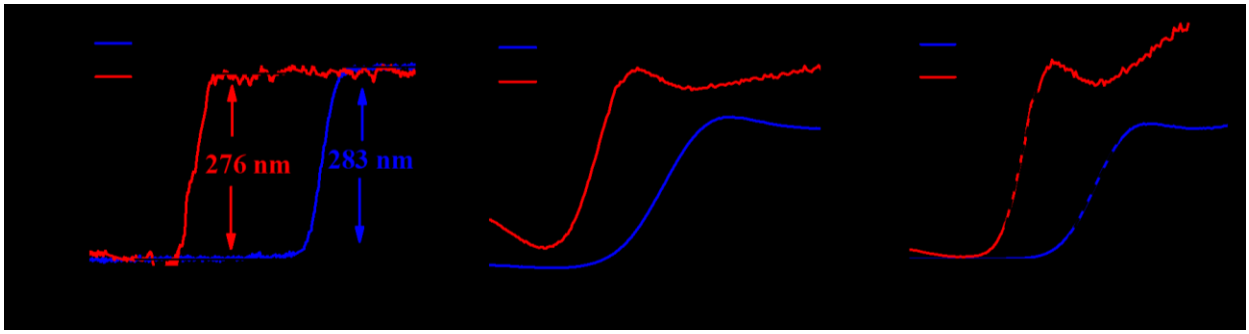

Figure 4

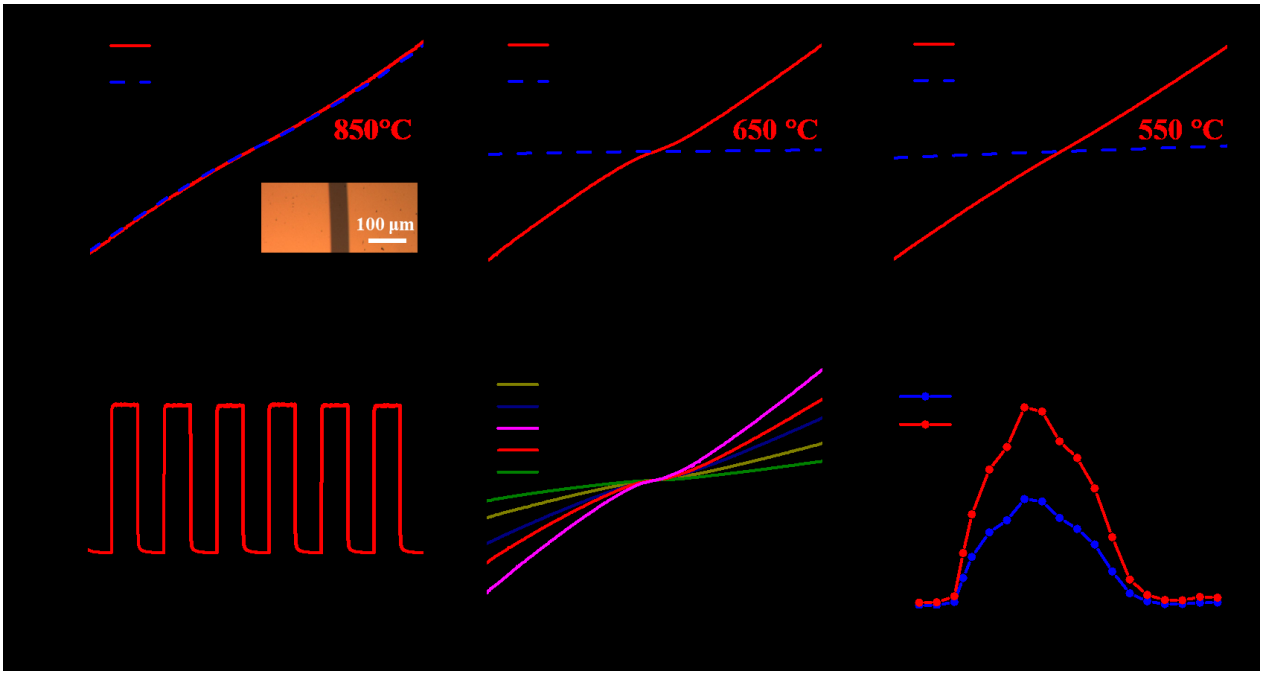

Figure 5

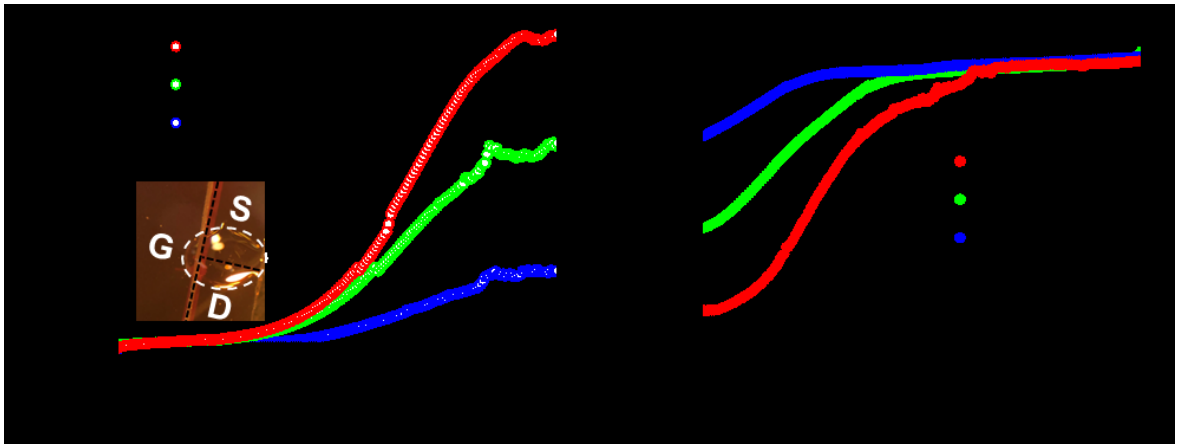

Figure 6